University of South Carolina

# Scholar Commons

# A Mathematical Model of a Hydrogen/Oxygen Alkaline Fuel Cell

Michael C. Kimble
*Texas A & M University - College Station*

Ralph E. White
*University of South Carolina - Columbia*, white@cec.sc.edu

Follow this and additional works at: https://scholarcommons.sc.edu/eche_facpub

Part of the Chemical Engineering Commons

# A Mathematical Model of a Hydrogen/Oxygen Alkaline Fuel Cell

Michael C. Kimble* and Ralph E. White**

*Center for Electrochemical Engineering, Department of Chemical Engineering, Texas A&M University, College Station, Texas 77843-3122*
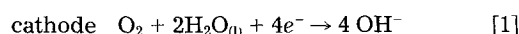
## ABSTRACT

A mathematical model of a hydrogen/oxygen alkaline fuel cell is presented that can be used to predict polarization behavior under various potential loads. The model describes the phenomena occurring in the solid, liquid, and gaseous phases of the anode, separator, and cathode regions, assuming a macrohomogeneous, three-phase porous electrode structure. The model calculates the spatial variation of the partial pressures of oxygen, hydrogen, and water vapor, dissolved oxygen and hydrogen concentrations, electrolyte concentration, and the solid- and solution-phase potential drops. By developing a complete model of the alkaline fuel cell, the interaction of the various transport and kinetic resistances can be more accurately investigated under conditions that simulate actual fuel cells. The model predicts that the solution-phase diffusional resistance of dissolved oxygen is a major limitation to achieving high performance at low cell potentials, while the ohmic drop in the solid electrodes contributes the most resistance at high cell potentials. Other limitations to achieving high power densities are indicated, and methods to increase the maximum attainable power density are suggested. These performance indications can help future research and the design of alkaline fuel cells.

The alkaline fuel cell (AFC) is capable of providing a clean, efficient, and high-powered source of electrical energy. The relative ease of operation, low weight and volume, and reliable performance have made the alkaline fuel cell an attractive power source for the American space program, as well as for electric vehicles, defense, stationary power sources, portable generators, and small submersibles, to name a few (1-3). However, for applications that require even higher power densities, the performance of the alkaline fuel cell needs to be improved. The maximum power density obtained from alkaline fuel cells has undergone many advances in recent years due to improved catalysts and electrode materials, and also due to optimized operating conditions and fuel cell design. It has been known that in order to increase the power density in AFCs, the activation, concentration, and ohmic polarizations should be minimized (4). For example, improved electrocatalysts for the oxygen reduction reaction in alkaline electrolytes has helped reduce the activation polarization (5); increased solid and solution conductivity has helped reduce the ohmic polarization (6); and dual-porosity electrodes have helped reduce concentration polarization (6-8). However, in order to investigate these phenomena, numerous and expensive experimental tests need to be performed. Furthermore, the interaction among the three types of polarization may cause difficulties in isolating the characteristics of a particular type of polarization. Mathematical modeling can help determine how changes in parameters and operating conditions will influence the various types of polarization, which subsequently affect the performance of a fuel cell. The AFC model can help identify parameters and concepts that limit the performance of the fuel cell based on today's state-of-the-art technology. Additionally, the model can be used to investigate the effects of hypothetical advances in technology on the predicted performance.

To serve as a basis for model development, a schematic of an alkaline fuel cell is presented in Fig. 1, showing the conceptualization of the three-phase electrodes. Typically, multilayer electrodes are used, where each electrode contains a gas diffusion region consisting of hydrophobic gaseous-filled pores, and a reaction region consisting of hydrophobic gas-filled pores as well as liquid-filled pores. The hydrophobicity in the electrodes is obtained by impregnating the porous electrodes with a wet-proofing agent such as Teflon, polytetrafluoroethylene (PTFE), or wax, which also serves as a binding material for the electrodes (6). The quantity and distribution of these wet-proofing agents have a strong effect on the fuel cell performance, as shown in Ref. (7, 9). The AFC operates by introducing either dry or humidified hydrogen and oxygen gases across the current collectors into the gas diffusion regions of the anode and cathode, respectively. Next, the gases diffuse into the reaction layers of the electrodes, where the gases can dissolve into the KOH electrolyte. In the middle of the fuel cell is a nonconducting microporous separator matrix which is assumed to prevent any gases from diffusing across the system. In some alkaline fuel cells, the electrolyte is circulated out of the system, which helps maintain a constant electrolyte concentration and assists in heat and water removal. A design constraint for this work is that the KOH electrolyte does not circulate outside the system. This will cause large electrolyte concentration variations across the electrodes and separator. In practical fuel cells, the liquid water produced in the system dilutes the KOH electrolyte to a certain extent. It is assumed that all electrochemically produced liquid water evaporates into the gas streams. This assumption is reasonable since in actual alkaline fuel cells the average electrolyte concentration reaches a constant value at steady state.

As the dissolved gases diffuse through the electrolyte, they react electrochemically according to the following reactions

$$\text{cathode} \quad O_2 + 2H_2O_{(l)} + 4e^- \rightarrow 4\,OH^- \qquad [1]$$

and

$$\text{anode} \quad H_2 + 2\,OH^- \rightarrow 2H_2O_{(l)} + 2e^- \qquad [2]$$
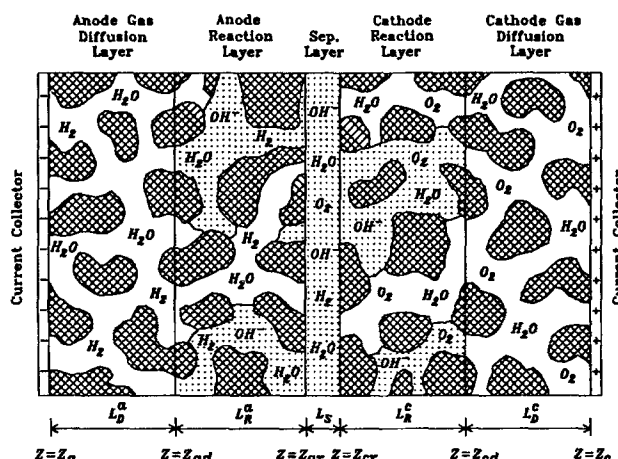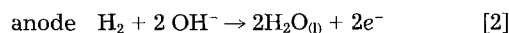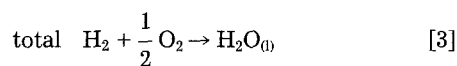


Fig. 1. Detailed schematic of the three-phase regions in a hydrogen/oxygen alkaline fuel cell.

* Electrochemical Society Student Member.
** Electrochemical Society Active Member.

Hence, the overall reaction is the production of water

$$\text{total} \quad H_2 + \frac{1}{2}O_2 \rightarrow H_2O_{(l)} \qquad [3]$$

with the simultaneous liberation of electrical energy. There have been numerous investigations into the mechanism of the oxygen reduction reaction in alkaline solutions. The two more common mechanisms for oxygen reduction involve the production of peroxide as either an intermediate species (10-13) or as a reaction product (14, 15). However, the kinetic parameters vary depending on the type of electrode substrate and electrocatalyst (5, 16-19), as well as on operating conditions such as concentration, pH, temperature, and oxygen partial pressure (20, 21). Therefore, since too many factors influence the oxygen reduction mechanism, it will be assumed that the direct four-electron transfer process, as given by Eq. [1], occurs in the oxygen electrode.

## Three-Phase Electrode Models

The need to increase current densities in electrochemical systems led to the development of three-phase electrodes (porous gas-diffusion electrodes) containing large interfacial surface areas between the solid electrocatalysts, electrolyte, and gaseous pores. However, since these electrodes contain a tortuous and nonuniform distribution of catalysts, gaseous-filled pores, and liquid-filled pores, it is difficult to describe accurately the phenomena occurring in the electrodes. Numerous experimental and modeling studies have been conducted over the years to describe and enhance the performance of these porous electrodes, as discussed in Ref. (22-26). The major difficulty in modeling three-phase porous electrodes is in describing the electrode structure. Most gas-diffusion electrodes incorporate a hydrophobic agent such as Teflon or PTFE mixed with the electrochemically active hydrophilic catalysts. This creates a stable three-phase boundary, but also creates a very complex wetting phenomenon, making it difficult to characterize the structure of the electrode.

One approach to describing three-phase electrodes is the agglomerate model (27-29), where the catalyst particles and liquid-filled pores coexist in a homogeneous continuum surrounded by the gaseous species. Giner's model (27) accounts for the diffusion of a dissolved gaseous species with electrochemical reaction in a cylindrical agglomerate and considers the variation in the solution phase potential. Unfortunately, the gas-phase and solid-phase resistances are not accounted for. The model predicts the performance of the electrode as a function of agglomerate radius and catalyst utilization for low current densities. Cutlip (30) developed an analytical model of the mass-transfer process occurring in gas diffusion electrodes. This model was primarily designed to study the mass-transfer effects due to low concentrations, taking into account gaseous diffusion, gas dissolution, and the transport of dissolved gas. Catalyst effectiveness factors were used to modify the electrocatalyst based on different shape factors. Cutlip concluded that the limiting current density is not influenced by the liquid-phase diffusional resistances. Another important conclusion from Cutlip's model is that the coupling of the gas-phase diffusional resistance and electrode thickness strongly influence the limiting current density. The limiting current density was found to be proportional to electrode thickness when the gas-phase diffusional resistances were nonexistent. Conversely, the limiting current density was found to be independent of electrode thickness when gas-phase diffusional resistances were present.

An improvement to Giner's flooded agglomerate model and to Cutlip's earlier model was presented by Iczkowski and Cutlip (31), who developed a fairly complete model of a three-phase electrode. This model accounted for the gaseous diffusion resistances, solution-phase diffusional resistances, and solid and liquid potential variations. They fitted their model to experimental polarization curves by adjusting the radius of the agglomerates, electrolyte film thickness, and the porosity-tortuosity factor of the gaseous

and liquid-filled pores. They applied their model to an air electrode in phosphoric acid up to current densities of 370 mA/cm$^2$ and concluded that ohmic resistance was the major cause of polarization losses in the electrode, followed by Knudsen and molecular diffusion effects. They also concluded that the solution-phase resistance of dissolved oxygen diffusion contributed the least to the polarization losses.

These single-electrode models have typically simplified or neglected various forms of resistance (*i.e.*, gas-phase diffusion, liquid-phase diffusion, electronic and ionic resistances). Some of these simplifications, such as a constant electrolyte concentration, are, as will be shown later, justified when a low overvoltage is applied, as was done in these models. However, at higher overvoltages, the assumptions of constant potentials and concentrations fail, since large potential and concentration gradients are formed. Thus, some of these three-phase models are not sufficient to predict high-power-density performance. Other investigations have been conducted into three-phase electrodes, in particular the oxygen electrode, since it is responsible for most of the polarization losses in AFCs. Unfortunately, no complete model of an alkaline fuel cell that contains both electrodes and the separator exists in the open literature. For this reason, it is difficult to generate any firm conclusions based on a single-electrode model when the interactions between the anode, cathode, and separator are not considered.

In order to investigate the performance of an alkaline fuel cell, the phenomena occurring in the separator and in the three phases of the electrodes need to be described. Including all regions of the cell allows the anode and cathode to interact through the continuous distribution of the solution-phase potential and the concentrations of the various species. This interaction is impossible to investigate with a single-electrode model. To account for the complexities of the microporous structures, porous electrode theory as described in Ref. (26) is used as a basis to describe the electrodes. This theory allows the superimposition of two or more phases into a single, homogeneous continuum. Thus, the gas-diffusion layers are described by a homogeneous continuum of gaseous-filled pores and solid electrode material. Similarly, the reaction layers can be described by superimposing the gaseous-filled and liquid-filled pores with the solid electrode particles.

To develop a complete model of the alkaline fuel cell, the various forms of resistance need to be considered. In the gas phase, the reactant gases (H$_2$ and O$_2$) diffuse via molecular diffusion through water vapor in their respective electrodes, contributing to the gas-phase diffusional resistances. Thus, the partial pressures of hydrogen ($P_{H_2}$), oxygen ($P_{O_2}$), and water vapor in the anode ($P_{H_2O}^a$) and cathode ($P_{H_2O}^c$) need to be determined. Electronic resistances occur through a potential drop in the anode ($E_a$) and cathode ($E_c$), while an ohmic resistance arises due to a varying solution-phase potential ($\phi$). To account for the liquid-phase diffusional resistances, the concentrations of dissolved hydrogen ($C_{H_2}$) and dissolved oxygen ($C_{O_2}$) need to be determined. The electrolyte concentration ($C_e$) varies in the solution phase, contributing to the ionic resistance. Additionally, the volume average velocity ($v^\blacksquare$) needs to be determined in order to consider convective effects in the solution phase. The fundamental equations needed to solve these eleven dependent variables will now be described in their general form. After these generalized equations have been applied in each region of the fuel cell, the necessary boundary conditions will be developed.

## Phenomenological Equations

A one-dimensional mathematical model of the alkaline fuel cell can be developed by considering conservation of mass and charge, transport of species, and reaction kinetics in each of the regions of the fuel cell as shown in Fig. 1. The equation of continuity for species $i$ can be written in the general form for a porous medium

$$\frac{\partial \epsilon C_i}{\partial t} = -\nabla \cdot N_i + R_i^p + R_i^e \ (i = O_2, H_2, H_2O, +, -, o) \quad [4]$$

where $R_i^p$ and $R_i^e$ represent rates of production for material that is "brought in" from across a phase boundary and for material that is produced from an electrochemical reaction, respectively. Since porous electrode theory is being used, the reaction rate terms are included throughout the electrode, as indicated in Eq. [4], instead of being treated as a boundary condition, as done in agglomerate models. Note that the $+$, $-$, and $\bigcirc$ species in Eq. [4] correspond to the $K^+$ ions, $OH^-$ ions, and solvent, respectively. Furthermore, the $\nabla$ operator in Eq. [4] and in subsequent equations is represented by $\partial/\partial z$, where $z$ is in the horizontal direction in reference to Fig. 1. The flux expression for species $i$, $N_i$, depends on whether species $i$ is in the gas or solution phase. In the gas phase, the Stefan-Maxwell equation can be simplified for a binary gas mixture of species $i$ and $j$ (32)

$$\nabla y_i = \sum_{j=1}^{2} \frac{RT}{P\mathfrak{D}_{i,j}^g} (y_i N_j - y_j N_i) \quad (i,j = O_2 \text{ or } H_2, H_2O) \quad [5]$$

where the effects of diffusion and convection are accounted for. The ionic flux expression (33)

$$N_i = -\mathfrak{D}_i^l \nabla C_i - z_i u_i F C_i \nabla\phi + C_i v^\blacksquare \quad (i = O_2, H_2, +, -, o) \quad [6]$$

can be used to represent the transport of species $i$ in the liquid-filled pores of the porous electrodes. This expression accounts for the diffusive, migration, and convective effects in the solution phase through the first, second, and third terms, respectively. Note that Eq. [5] and [6] contain effective diffusivities, $\mathfrak{D}_i$, which are related to the free stream diffusivities by a porosity and tortuosity factor

$$\mathfrak{D}_i = \frac{\epsilon D_i}{\tau} \quad [7]$$

and the Nernst-Einstein relation is assumed to relate the mobility, $u_i$, to the diffusivity of species $i$

$$u_i = \frac{\mathfrak{D}_i^l}{RT} \quad [8]$$

The electrochemical reaction rate per unit of electrode volume, $R_i^e$, is expressed for species $i$ in the form

$$R_i^e = -\frac{s_i a^l i}{nF} \quad [9]$$

where the stoichiometric coefficients, $s_i$, are given by expressing the electrochemical reactions in the form

$$\sum_i s_i M^{z_i} \rightarrow ne^- \quad [10]$$

The local current density, $i$, is expressed by the Butler-Volmer electrochemical rate expression

$$i = i^o \left[ \prod_i \left( \frac{C_1}{C_i^r} \right)^{p_1} \exp\left( \frac{\alpha_a nF}{RT} \eta \right) \right.$$
$$\left. - \prod_i \left( \frac{c_1}{C_i^r} \right)^{q_i} \exp\left( \frac{-\alpha_c nF}{RT} \eta \right) \right] \quad [11]$$

where the overpotential, $\eta$, is given by

$$\eta = E - \phi - U_{\text{ref}} \quad [12]$$

Note that Eq. [11] is used for the hydrogen oxidation and oxygen reduction reactions rather than Tafel expressions in order to account for the effects of the reactant and product concentrations over the entire range of potentials investigated.

The rate of production of hydrogen and oxygen gas into the electrolyte across a phase boundary, $R_i^p$, is approximated by

$$R_i^p = -a^g \mathfrak{D}_i^l \left( \frac{H_i P_i - C_i}{\delta} \right) \quad [13]$$

where $H_i$ is Henry's law constant in $\text{mol}/(\text{cm}^3\text{atm})$ for species $i$, $\delta$ is the diffusion layer thickness, and $a^g$ is the specific surface area of the gaseous pores. This rate expression assumes that equilibrium will be established at the gas-liquid interface following a Henry's law expression. These equations describe the physical phenomena believed to be occurring in the alkaline fuel cell and will now be applied to the specific regions of the fuel cell.

*Gas-diffusion regions.*—Each electrode contains a gas-diffusion layer to prevent the electrolyte from weeping into the gas stream and to provide structural support to the electrode. It may be assumed that the hydrophobicity of the electrode will prevent any liquid from entering this region. Therefore, only hydrogen gas and water vapor will exist in the anode gas-diffusion layer, and only oxygen gas and water vapor will exist in the cathode gas-diffusion layer. Additionally, the solid electrode material in the gas diffusion regions will experience an ohmic drop that follows Ohm's law. Hence, each gas-diffusion region has three unknown variables: $P_{H_2}$, $P_{H_2O}^a$, and $E_a$ for the anode layer, and $P_{O_2}$, $P_{H_2O}^c$, and $E_c$ for the cathode gas diffusion layer. In the gas-diffusion regions, the reactant gases ($H_2$ or $O_2$) diffuse through water vapor from the gas channel/gas diffusion interface to the gas diffusion/reaction interface. The water vapor in these regions comes from two sources: water vapor that enters the system with the reactant gases and the water vapor that evaporates from the electrolyte in the gas reaction regions. Thus, the water vapor itself can diffuse in or out of the gas diffusion regions depending on the inlet and reaction conditions. To account properly for the relative fluxes of reactant gas to water vapor needed in the Stefan-Maxwell expression, Eq. [5], a water balance is needed about the system. From the stoichiometry of the overall reaction, Eq. [3], the flux of hydrogen gas is related to the total flux of water leaving the system

$$N_{H_2}^g = -N_{H_2O}^T \quad [14]$$

and similarly for oxygen gas

$$N_{O_2}^g = -\frac{1}{2} N_{H_2O}^T \quad [15]$$

Since the total flux of water vapor is simply the sum of the water fluxes that leave with the anode and cathode gas streams

$$N_{H_2O}^T = N_{H_2O}^a + N_{H_2O}^c \quad [16]$$

then a water fraction, $f_a$, can be defined that relates the amount of water that leaves through the anode to the total amount of water generated (34)

$$f_a = \frac{N_{H_2O}^a}{N_{H_2O}^a + N_{H_2O}^c} \quad [17]$$

Similarly, a cathode fraction ($f_c = 1 - f_a$) can be defined which gives

$$f_a = 1 - \frac{N_{H_2O}^c}{N_{H_2O}^a + N_{H_2O}^c} \quad [18]$$

Equations [14], [16], and [17] can be combined to relate the flux of hydrogen gas to the flux of water vapor in the anode

$$N_{H_2O}^a = -f_a N_{H_2}^g \quad [19]$$

Similarly, Eq. [15], [16], and [18] can be combined to give the relationship between the oxygen and water vapor flux in the cathode

$$N_{H_2O}^c = -2(1 - f_a)N_{O_2}^g \quad [20]$$

These flux ratios can be inserted into the convective term of the Stefan-Maxwell flux expression, Eq. [5], and combined with the equation of continuity at steady state, Eq. [4] (where $R_i^p$ and $R_i^c$ are zero since there are no reactions in this region), to give

$$\nabla \cdot \left[ \frac{\mathfrak{D}_{H_2}^g P^a}{P_{H_2O}^a + f_a P_{H_2}} \nabla P_{H_2} \right] = 0 \quad [21]$$

in the anode and

$$\nabla \cdot \left[ \frac{\mathfrak{D}_{O_2}^g P^c}{P_{H_2O}^c + 2(1 - f_a)P_{O_2}} \nabla P_{O_2} \right] = 0 \qquad [22]$$

in the cathode. Since no production or consumption of any kind occurs in the gas-diffusion layers, the total pressure will be constant in each region

$$P^a = P_{H_2} + P_{H_2O}^a \qquad [23]$$

in the anode and

$$P^c = P_{O_2} + P_{H_2O}^c \qquad [24]$$

in the cathode.

The last dependent variables that need to be determined in the gas-diffusion regions are the anode and cathode solid potentials, $E_a$ and $E_c$, respectively. The ohmic drop in these regions can be described by Ohm's law

$$\nabla E = -\frac{I}{\sigma} \qquad [25]$$

where $\sigma$ is the conductivity of the electrode and $I$ is the total cell current density. Since there are no electrochemical reactions in the gasdiffusion region, the current density is constant, so that the gradient of the current density is zero. Hence, the ohmic drop in the anode gas-diffusion layer is given by

$$\nabla^2 E_a = 0 \qquad [26]$$

and similarly in the cathode gas diffusion region

$$\nabla^2 E_c = 0 \qquad [27]$$

In summary, the governing equations for the anode gas-diffusion region are given by Eq. [21], [23], and [26]. Similarly, the governing equations for the cathode gas-diffusion region are given by [22], [24], and [27].

*Gas reaction regions.*—In addition to containing a gas-diffusion layer, each electrode has a gas reaction layer where the electrochemical and dissolution reactions occur. The reactant gases ($O_2$ or $H_2$) diffuse through water vapor in the gas-filled pores of the electrode, while some of the gases dissolve into the liquid-filled pores. The dissolved gases further diffuse in the solution until they reach a reaction site where they react electrochemically. The electrochemical reactions are influenced by the electrolyte concentration, solution potential, solid electrode potentials, volume average velocity, and dissolved reactant gas concentrations. Thus, in the anode gas reaction region there are seven variables to solve for: $C_e$, $\phi$, $E_a$, $C_{H_2}$, $v^{\blacksquare}$, $P_{H_2}$, and $P_{H_2O}^a$. Similarly, there are seven unknown variables in the cathode gas reaction region: $C_e$, $\phi$, $E_c$, $C_{O_2}$, $v^{\blacksquare}$, $P_{O_2}$, and $P_{H_2O}^c$. The reactant gases in these layers will have the same flux expressions as developed in the gas-diffusion regions. Since the gases dissolve into the electrolyte, the gas dissolution rates are included in the equation of continuity. Combining Eq. [4], [5], and [13] gives an expression for the hydrogen gas pressure at steady state in the anode

$$\nabla \cdot \left( \frac{\mathfrak{D}_{H_2}^g (P_{H_2O}^a + P_{H_2})}{P_{H_2O}^a + f_a P_{H_2}} \nabla P_{H_2} \right)$$

$$- a_a^g \mathfrak{D}_{H_2}^l RT \left( \frac{H_{H_2} P_{H_2} - C_{H_2}}{\delta_a} \right) = 0 \qquad [28]$$

and an expression for the steady-state oxygen gas-pressure distribution in the cathode

$$\nabla \cdot \left( \frac{\mathfrak{D}_{O_2}^g (P_{H_2O}^c + P_{O_2})}{P_{H_2O}^c + 2(1 - f_a)P_{O_2}} \nabla P_{O_2} \right)$$

$$- a_c^g \mathfrak{D}_{O_2}^l RT \left( \frac{H_{O_2} P_{O_2} - C_{O_2}}{\delta_c} \right) = 0 \qquad [29]$$

In order to account for the evaporation of water into the gaseous pores, linear correlations were developed to give the partial pressure of water as a function of KOH concentration and temperature based on data from (35). At the base-case temperature of 80°C, this correlation is adequately described by

$$P_{H_2O} = 0.46858 - 28.095 \cdot C_{KOH} \qquad [30]$$

Since the electrolyte concentration varies in the liquid pores of the gas reaction regions, the water vapor pressure will also vary as given by Eq. [30], and will influence the gas-phase transport as given by Eq. [28] and [29]. Note that these correlations assume that equilibrium will be established between the gas and liquid phases in the gas reaction regions.

The dissolved reactant gas concentrations are given by combining Eq. [4], [6], [9], and [13] to give (at steady state)

$$\mathfrak{D}_{H_2}^l \nabla^2 C_{H_2} - \nabla \cdot (v^{\blacksquare} C_{H_2}) + \frac{i_a a_a^l}{2F}$$

$$+ a_a^g \mathfrak{D}_{H_2}^l \left[ \frac{H_{H_2} P_{H_2} - C_{H_2}}{\delta_a} \right] = 0 \qquad [31]$$

for the dissolved hydrogen concentration in the anode gas reaction region and

$$\mathfrak{D}_{O_2}^l \nabla^2 C_{O_2} - \nabla \cdot (v^{\blacksquare} C_{O_2}) + \frac{i_c a_c^l}{4F}$$

$$+ a_c^g \mathfrak{D}_{O_2}^l \left[ \frac{H_{O_2} P_{O_2} - C_{O_2}}{\delta_c} \right] = 0 \qquad [32]$$

for the dissolved oxygen concentration in the cathode gas reaction region. The local current densities in Eq. [31] and [32] are expressed using the Butler-Volmer kinetic expression, Eq. [11]

$$i_a = i_a^o \left[ \left( \frac{C_{H_2}}{C_{H_2}^r} \right)^{pH_2} \left( \frac{C_e}{C_e^r} \right)^{pe} \exp \left( \frac{\alpha_a^a n_a F}{RT} (E_a - \phi - U_a) \right) \right]$$

$$- i_a^o \left[ \exp \left( -\frac{\alpha_c^a n_a F}{RT} (E_a - \phi - U_a) \right) \right] \qquad [33]$$

for the anodic current density and

$$i_c = i_c^o \left[ \left( \frac{C_e}{C_e^r} \right)^{pe} \exp \left( \frac{\alpha_c^c n_c F}{RT} (E_c - \phi - U_c) \right) \right]$$

$$- i_c^o \left[ \left( \frac{C_{O_2}}{C_{O_2}^r} \right)^{qO_2} \exp \left( -\frac{\alpha_c^c n_c F}{RT} (E_c - \phi - U_c) \right) \right] \qquad [34]$$

for the cathodic current density. The superscribed $r$ variables pertain to the reference concentrations associated with either the cathodic, $i_c^o$, or anodic, $i_a^o$, exchange current densities. The reference potentials, $U$, for each electrochemical reaction are given as a function of temperature, electrolyte concentration, and the partial pressure of the reactant gas relative to a standard reversible hydrogen electrode as defined by (36)

$$U = U^\theta - \frac{RT}{nF} \sum_i s_i \ln \left( \frac{C_i}{\rho} \right) - U_{RE}^\theta$$

$$+ \frac{RT}{n_{RE}F} \sum_i s_{i,RE} \ln \left( \frac{C_{i,RE}}{\rho} \right) \qquad [35]$$

where $U^\theta$ is the standard potential at temperature $T$ and $U_{RE}^\theta$ is the reference potential, both relative to the standard hydrogen electrode, which is defined to be zero for convenience. Hence, these reference potentials are

$$U_c = U_c^\theta - \frac{8.314T}{4F} \ln \left( \frac{C_e^4}{P_{O_2}} \right) (V) \qquad [36]$$

for the cathode and

$$U_a = U_a^\theta - \frac{8.314T}{2F} \ln (P_{H_2} C_e^2) \text{ (V)} \qquad [37]$$

for the anode. The standard electrode potentials at temperature $T$ are given by (37)

$$U_c^\theta = 0.4011 - (T - 298.15)1.682 \times 10^{-3} \text{ (V)} \qquad [38]$$

and

$$U_a^\theta = -0.828 - (T - 298.15)8.360 \times 10^{-4} \text{ (V)} \qquad [39]$$

The concentrations of the ionic species, $K^+$ and $OH^-$, are expressed by combining the material balance, Eq. [4], the ionic flux, Eq. [6], and the electrochemical rate, Eq. [9]. Combining these equations for each ionic species gives

$$\mathcal{D}_+\nabla^2 C_+ + u_+ F \nabla \cdot (C_+ \nabla\phi) - \nabla \cdot (v^\blacksquare C_+) = 0 \qquad [40]$$

for the $K^+$ ions and

$$\mathcal{D}_-\nabla^2 C_- - \frac{ia^l}{F} - u_- F \nabla \cdot (C_- \nabla\phi) - \nabla \cdot (v^\blacksquare C_-) = 0 \qquad [41]$$

for the $OH^-$ ions in both the anode and cathode gas reaction regions. In Eq. [41], the $ia^l$ term is given by $i_a a_a^l$ for the anodic gas reaction region and by $i_c a_c^l$ for the cathodic gas reaction region. The electroneutrality condition

$$\sum_i z_i C_i = 0 \qquad [42]$$

can be used to relate the potassium and hydroxide ion concentrations in the solution phase, giving

$$C_e = C_- = C_+ \qquad [43]$$

Equation [43] can be combined with Eq. [40] and [41] to eliminate the $K^+$ and $OH^-$ ion concentrations, giving

$$\mathcal{D}_+\nabla^2 C_e + u_+ F \nabla \cdot (C_e \nabla\phi) - \nabla \cdot (v^\blacksquare C_e) = 0 \qquad [44]$$

and

$$\mathcal{D}_-\nabla^2 C_e - \frac{ia^l}{F} - u_- F \nabla \cdot (C_e \nabla\phi) - \nabla \cdot (v^\blacksquare C_e) = 0 \qquad [45]$$

for the anode and cathode gas reaction regions.

An expression for the volume-average velocity can be formulated by first multiplying the equation of continuity, Eq. [4], for each species $i$ present in the solution by the partial molar volume (assumed constant) of each species

$$\bar{V}_i \frac{\partial \epsilon^l C_i}{\partial t} = [-\nabla \cdot N_i + R_i^e + R_i^p]\bar{V}_i \ (i = +, -, o, O_2, H_2) \qquad [46]$$

and summed over all species resulting in

$$\frac{\partial[\epsilon^l(\bar{V}_- C_- + \bar{V}_+ C_+ + \bar{V}_o C_o + \bar{V}_{H_2} C_{H_2} + \bar{V}_{O_2} C_{O_2})]}{\partial t}$$

$$= -\nabla \cdot (N_- \bar{V}_- + N_+ \bar{V}_+ + N_o \bar{V}_o + N_{O_2} \bar{V}_{O_2} + N_{H_2} \bar{V}_{H_2})$$

$$+ R_-^e \bar{V}_- + R_+^e \bar{V}_+ + R_o^e \bar{V}_o + R_{O_2}^p \bar{V}_{O_2} + R_{H_2}^p \bar{V}_{H_2} \qquad [47]$$

Recognizing that

$$1 = \bar{V}_- C_- + \bar{V}_+ C_+ + \bar{V}_o C_o + \bar{V}_{H_2} C_{H_2} + \bar{V}_{O_2} C_{O_2} \qquad [48]$$

and assuming that the partial molar volumes for oxygen and hydrogen are much smaller than for the electrolyte species, then Eq. [47] can be simplified to

$$\frac{\partial \epsilon^l}{\partial t} = -\nabla \cdot (N_- \bar{V}_- + N_+ \bar{V}_+ + N_o \bar{V}_o)$$

$$+ R_-^e \bar{V}_- + R_+^e \bar{V}_+ + R_o^e \bar{V}_o \qquad [49]$$

The volume average velocity, $v^\blacksquare$, defined by (32) is given as

$$v^\blacksquare = \sum_i C_i v_i \bar{V}_i = \sum_i N_i \bar{V}_i \qquad [50]$$

which can be inserted into Eq. [49] and combined with Eq. [9] to give

$$\frac{\partial \epsilon^l}{\partial t} = -\nabla \cdot v^\blacksquare - (s_- \bar{V}_- + s_+ \bar{V}_+ + s_o \bar{V}_o) \frac{ia^l}{nF} \qquad [51]$$

Newman and Chapman (38) make the following assumption for a binary electrolyte

$$\nu_+ t_+^o \bar{V}_+ = \nu_- t_-^o \bar{V}_- \qquad [52]$$

which can be combined with

$$1 = t_-^o + t_+^o \qquad [53]$$

and the partial molar volume of the electrolyte

$$\bar{V}_e = \nu_+ \bar{V}_+ + \nu_- \bar{V}_- \qquad [54]$$

to give

$$t_+^o \bar{V}_e = \nu_- \bar{V}_- \qquad [55]$$

and

$$t_-^o \bar{V}_e = \nu_+ \bar{V}_+ \qquad [56]$$

Combining Eq. [53], [55], and [56] with the number of electrons transferred

$$-n = s_+ z_+ + s_- z_- \qquad [57]$$

gives an expression relating the partial molar volume of the electrolyte to its dissociated ions

$$s_- \bar{V}_- + s_+ \bar{V}_+ = \frac{s_- \bar{V}_e}{\nu_-} + \frac{t_-^o \bar{V}_e n}{\nu_- z_-} \qquad [58]$$

Since the liquid-phase porosity does not change with time for the type of electrochemical reactions occurring in the alkaline fuel cell, the time rate of change of the liquid-phase porosity is zero. Thus, combining Eq. [51] and [58] gives an expression for the volume-average velocity

$$\nabla \cdot v^\blacksquare = -\left(\frac{s_- \bar{V}_e}{\nu_-} + \frac{t_-^o \bar{V}_e n}{\nu_- z_-} + s_o \bar{V}_o\right) \frac{ia^l}{nF} \qquad [59]$$

Since the total current density obtained from the fuel cell is equal to the integral of the local current densities as generated by the electrochemical reaction, then

$$I = -\int_0^{L_R} ia^l dz \qquad [60]$$

Differentiating Eq. [25] and [60] and combining gives an expression for the anode potential drop in the anodic gas reaction region

$$\nabla^2 E_a = \frac{i_a a_a^l}{\sigma_a} \qquad [61]$$

and for the cathodic potential drop in the cathode gas reaction layer

$$\nabla^2 E_c = \frac{i_c a_c^l}{\sigma_c} \qquad [62]$$

where the anodic and cathodic current density expressions are given by Eq. [33] and [34], respectively. In summary, the seven governing equations for the anode gas reaction region are Eq. [28], [30], [31], [44], [45], [59], and [61]. The seven governing equations for the cathode gas reaction region are Eq. [29], [30], [32], [44], [45], [59], and [62].

*Separator.*—In the middle of the alkaline fuel cell there is a porous separator matrix that is assumed to contain

only solid nonconducting material and liquid-filled pores. The separator allows the ionic and dissolved reactant species to diffuse between the anode and cathode regions. The five unknown variables in this region are $C_e$, $\phi$, $v^\blacksquare$, $C_{O_2}$, and $C_{H_2}$. The same development previously presented for the ionic species in the gas reaction regions can be applied here. No electrochemical reactions occur in the separator, thus Eq. [44] and [45] simplify to

$$\mathcal{D}_+ \nabla^2 C_e + u_+ F \nabla \cdot (C_e \nabla \phi) - \nabla \cdot (v^\blacksquare C_e) = 0 \qquad [63]$$

and

$$\mathcal{D}_- \nabla^2 C_e - u_- F \nabla \cdot (C_e \nabla \phi) - \nabla \cdot (v^\blacksquare C_e) = 0 \qquad [64]$$

Unreacted dissolved gases from the gas reaction regions may diffuse into the separator. Combining Eq. [4] and [6] and simplifying gives the steady-state dissolved hydrogen concentration distribution

$$\mathcal{D}_{H_2}^l \nabla^2 C_{H_2} - \nabla \cdot (v^\blacksquare C_{H_2}) = 0 \qquad [65]$$

and the dissolved oxygen concentration variation

$$\mathcal{D}_{O_2}^l \nabla^2 C_{O_2} - \nabla \cdot (v^\blacksquare C_{O_2}) = 0 \qquad [66]$$

The volume-average velocity can be simplified from Eq. [59] by recognizing that the local current density term is zero in the separator, giving

$$\nabla \cdot v^\blacksquare = 0 \qquad [67]$$

In summary, the five governing equations for the separator are given by Eq. [63], [64], [65], [66], and [67].

## Boundary Conditions

There are six boundaries in the alkaline fuel cell that need to be incorporated into the model. Referring to Fig. 1, these boundaries occur at the following interfaces: anode gas channel/anode gas-diffusion layer ($z_a$), anode gas-diffusion layer/anode gas reaction layer ($z_{ad}$), anode gas reaction layer/separator layer ($z_{ar}$), separator layer/cathode gas reaction layer ($z_{cr}$), cathode gas reaction layer/cathode gas-diffusion layer ($z_{cd}$), and cathode gas-diffusion layer/cathode gas channel ($z_c$). Dirichlet or Neumann-type boundary conditions can be used to describe the phenomena that occur at these interfaces. These conditions will now be presented at each interface.

*Anode gas channel/anode gas-diffusion interface.*—The boundaries at this interface follow the Dirichlet-type conditions where the gaseous hydrogen and water vapor pressures are fixed values. Since the total pressure at this interface remains constant, the partial pressures of hydrogen and water will vary so that the flux of water in the anode, Eq. [19], will be consistent with the fraction, $f_a$, and the total flux of water predicted by the cell current density

$$N_{H_2O}^T = \frac{I_{cell}}{2F} \qquad [68]$$

Hence, the water vapor pressure at this interface can be calculated by combining Eq. [5], [14], [19], and [68] and solving for the water vapor pressure at the interface. For the total pressure to remain constant, the hydrogen pressure is then given by

$$P_{H_2} = P^a - P_{H_2O}^a \qquad [69]$$

Since the model predicts the current for a given potential load, the anode potential at this interface can be arbitrarily set to any value. Hence, the anode potential, $E_a$, was set to zero at this interface.

*Anode gas diffusion/anode gas reaction interface.*—At this interface, boundary conditions are needed for seven unknown variables: $P_{H_2}$, $P_{H_2O}^a$, $E_a$, $C_{H_2}$, $C_e$, $\phi$, and $v^\blacksquare$. The flux for the hydrogen gas as given by Eq. [5] and [14] is continuous at this interface, giving

$$\mathcal{D}_{H_2}^g \nabla P_{H_2}|_D = \mathcal{D}_{H_2}^g \nabla P_{H_2}|_R \qquad [70]$$

The partial pressure of water at this interface is given by the correlation developed earlier for the partial pressure of

water above a KOH electrolyte, Eq. [30]. The faradaic current density is continuous at this boundary, as given by Eq. [25], resulting in

$$\sigma_D \nabla E_a|_D = \sigma_R \nabla E_a|_R \qquad [71]$$

The fluxes for the dissolved hydrogen and the $K^+$ and $OH^-$ ions are zero, since there exists a solution/solid phase interface at this boundary. Setting the ionic flux expression, Eq. [6], to zero for each of these species results in

$$0 = \nabla C_e|_R \qquad [72]$$

$$0 = \nabla \phi|_R \qquad [73]$$

and

$$0 = \nabla C_{H_2}|_R \qquad [74]$$

The volume average velocity at this interface is given by Eq. [59], where the local current density is zero, since no electrochemical reactions take place at this interface. Also, since this boundary is a solid/solution-phase interface, the volume-average velocity has to be zero. Hence

$$0 = \nabla v^\blacksquare|_R \quad \text{and} \quad v^\blacksquare = 0 \qquad [75]$$

*Anode gas reaction/separator interface.*—Eight boundary conditions need to be specified at this interface: for $P_{H_2}$, $P_{H_2O}^a$, $E_a$, $C_{H_2}$, $C_e$, $\phi$, $v^\blacksquare$, and $C_{O_2}$. Since hydrogen gas does not enter the separator, the flux of hydrogen gas, Eq. [5], is set to zero, giving

$$\nabla P_{H_2}|_R = 0 \qquad [76]$$

and the partial pressure of water is again given by Eq. [30]. The faradaic current is zero at this boundary condition, since the separator is nonconductive, which simplifies from Eq. [25] to give

$$\nabla E_a|_R = 0 \qquad [77]$$

The fluxes for the electrolyte species and dissolved hydrogen are continuous at this interface. Equating Eq. [6] as applied in the reaction layer and the separator layer for each species gives

$$\mathcal{D}_{H_2}^l \nabla C_{H_2}|_R = \mathcal{D}_{H_2}^l \nabla C_{H_2}|_S \qquad [78]$$

$$-\mathcal{D}_+ \nabla C_e|_R - u_+ F C_e \nabla \phi|_R = -\mathcal{D}_+ \nabla C_e|_S - u_+ F C_e \nabla \phi|_S \qquad [79]$$

and

$$-\mathcal{D}_- \nabla C_e|_R + u_- F C_e \nabla \phi|_R = -\mathcal{D}_- \nabla C_e|_S + u_- F C_e \nabla \phi|_S \qquad [80]$$

The volume-average velocity at this interface is given by equating Eq. [59] as applied in the anode gas reaction layer to that applied in the separator region. Note that the local current density term is zero since no electrochemical reactions occur at this boundary

$$\nabla v^\blacksquare|_R = \nabla v^\blacksquare|_S \qquad [81]$$

Unreacted dissolved oxygen in the cathode gas reaction layer can diffuse through the separator toward the anode gas reaction layer. Any dissolved oxygen in the anode gas reaction layer would be quickly consumed by an electrochemical reaction and would not significantly influence the system at all. Hence, the dissolved oxygen concentration can be set to zero at the anode reaction layer/separator interface

$$0 = C_{O_2}|_S \qquad [82]$$

*Separator/cathode gas reaction interface.*—Similar conditions are used at this interface as used at the anode gas reaction layer/separator interface. Hence, eight boundary conditions can be developed for: $P_{O_2}$, $P_{H_2O}^c$, $E_c$, $C_{O_2}$, $C_e$, $\phi$, $v^\blacksquare$, and $C_{H_2}$. These variables will follow the same form of the equations developed for the anode reaction/separator interface.

*Cathode gas reaction/cathode gas-diffusion interface.*—The boundary conditions at this interface are analogous to those at the anode gas-diffusion/anode gas reaction interface. Thus, seven boundary conditions for $P_{O_2}$, $P_{H_2O}^c$, $E_c$, $C_{O_2}$, $C_e$, $\phi$, and $v^\blacksquare$ can be described accordingly.

*Cathode gas-diffusion/cathode gas channel interface.*— The boundary conditions at this interface are similar to those at the anode gas channel/anode gas-diffusion interface except that the cathode potential is set to the applied cell potential. The partial pressures of oxygen and water are, again, allowed to vary at this boundary in an analogous manner, as shown at the anode channel/gas diffusion interface.

## Model Parameters

The alkaline fuel cell model requires various parameters that are specific to the cell structure, electrochemical reactions, and operating conditions. Table I shows the electrochemical parameters used for the anode and cathode reactions for the base case conditions. The number of electrons transferred, charge numbers, and the stoichiometric coefficients for the cathode and anode reactions were taken from reactions [1] and [2], respectively, with the reactions following the form of Eq. [10]. Since the electrolyte is KOH, the dissociation constants of the ionic species are 1. The transfer coefficients for the hydrogen oxidation reaction in Table I were estimated based on reported Tafel slopes of about 0.12 for the hydrogen evolution reaction (39). For the hydrogen evolution reaction, the Tafel slope, $b$, is

$$b = 2.3 \frac{RT}{\alpha_c^a n_a F} \qquad [83]$$

giving $\alpha_c^a n_a$ of about 0.5. Assuming that

$$\alpha_a n + \alpha_c n = n \qquad [84]$$

then the product of the number of electrons transferred and the anodic transfer coefficient would be 1.5, as shown in Table I. Note that this assumes the mechanism for hydrogen oxidation and hydrogen reduction are the same. For the oxygen reduction reaction, the transfer coefficients are based on experimentally measured Tafel slopes of about 0.045 (40), giving the transfer coefficients shown in Table I. Since reliable transfer coefficient data are not readily available for various temperatures, concentrations, potentials, and electrocatalysts, these transfer coefficients are assumed constant. Table I also shows four adjustable parameters: the anodic and cathodic exchange transfer currents ($i_a^0 \cdot a_a^l$ and $i_c^0 \cdot a_c^l$) and the anodic and cathodic diffusional film areas ($a_a^g/\delta_a$ and $a_c^g/\delta_c$). For the base case conditions, these parameters were selected to give performance curves similar to those obtained experimentally. As will be shown later, these parameters can be adjusted to fit the model to experimental polarization data. The base-case operating conditions are shown in Table II, where $E_{cell}$ corresponds to the set cell potential. Table III shows the structural and electrode parameters common to both the anode and cathode for the base-case conditions. These parameters were selected as being representative of actual alkaline fuel cells.

**Table I. Electrochemical parameters for the anode and cathode reactions (base-case conditions).**

| Anode | | Cathode | |
|---|---|---|---|
| Parameter | Value | Parameter | Value |
| $n_a$ | 2 | $n_c$ | 4 |
| $s_{H2}$ | 1 | $s_{O2}$ | −1 |
| $s_-$ | 2 | $s_-$ | 4 |
| $s_o$ | −2 | $s_o$ | −1 |
| $z_-$ | −1 | $z_-$ | −1 |
| $z_+$ | 1 | $z_+$ | 1 |
| $\nu_-$ | 1 | $\nu_-$ | 1 |
| $\nu_+$ | 1 | $\nu_+$ | 1 |
| $p_{H2}$ | 2 | $q_{O2}$ | 0.5 |
| $p_e$ | 2.0 | $p_e$ | 2.0 |
| $\alpha_a^a n_a$ | 1.5 | $\alpha_a^c n_c$ | 2.5 |
| $\alpha_c^a n_a$ | 0.5 | $\alpha_c^c n_c$ | 1.5 |
| $i_a^0 \cdot a_a^l$ | 0.60 A/cm$^3$ | $i_c^0 \cdot a_c^l$ | 0.60 A/cm$^3$ |
| $a_a^g/\delta_a$ | $5 \times 10^8$ cm$^{-2}$ | $a_c^g/\delta_c$ | $5 \times 10^8$ cm$^{-2}$ |

**Table II. Base-case operating conditions.**

| Parameter | Value |
|---|---|
| Initial electrolyte concentration, $C_e$ | $7N$ |
| Temperature, $T$ | 80°C |
| Inlet anode gas pressure, $P^a$ | 4.1 atm |
| Inlet cathode gas pressure, $P^c$ | 4.1 atm |
| Applied anode potential, $E_a$ | 0.0 V |
| Applied cathode potential, $E_c$ | $E_{cell}$ |

**Table III. Structural and electrode parameters for the anode and cathode base-case conditions.**

| Parameter | Value | Parameter | Value |
|---|---|---|---|
| $L_D$ | 0.0250 cm | $C_e^r$ | $7.0 \times 10^{-3}$ mol/cm$^3$ |
| $L_R$ | 0.0050 cm | $C_{O2}^r$ | $3.196 \times 10^{-8}$ mol/cm$^3$ |
| $L_S$ | 0.0050 cm | $C_{H2}^r$ | $4.802 \times 10^{-8}$ mol/cm$^3$ |
| $\sigma_D$ | 5.0 S/cm$^2$ | $\bar{V}_e$ | 18.591 cm$^3$/mol |
| $\sigma_R$ | 5.0 S/cm$^2$ | $\bar{V}_o$ | 17.888 cm$^3$/mol |
| $\epsilon_D^g$ | 0.70 | $t_-^0$ | 0.696 |
| $\epsilon_R^g$ | 0.05 | $\tau_a$ | 1.2 |
| $\epsilon_R^l$ | 0.65 | $\tau_c$ | 1.2 |
| $\epsilon_S$ | 0.80 | $\tau_s$ | 1.0 |

In order to obtain realistic performance of the alkaline fuel cell, the diffusion rates of the various species were determined as a function of concentration (or pressure) and temperature. This was necessary to accommodate the changing pressure in the electrodes and the varying electrolyte concentration across the system. The gas-phase diffusivities of oxygen in water and hydrogen in water as a function of temperature and pressure were based on corresponding-states principles (32), giving

$$D_{O2}^g = \frac{4.2076 \times 10^{-7} T^{2.334}}{P} \, cm^2/s \qquad [85]$$

and

$$D_{H2}^g = \frac{2.1410 \times 10^{-6} T^{2.334}}{P} \, cm^2/s \qquad [86]$$

Correlations were developed for the diffusivities of dissolved oxygen and dissolved hydrogen in KOH as a function of temperature and concentration based on experimental measurements (41).

The ionic equivalent conductances were determined by scaling the equivalent conductances of the KOH electrolyte at 25°C (42)

$$\Lambda = 272.0\text{-}3846.59 C_e^{0.5} + 1.41$$
$$\times 10^5 \, C_e(1.0\text{-}7.191 \, C_e^{0.5}) \, (cm^2/eq. \, \Omega) \quad [87]$$

to the temperature of interest by using the ratio of the limiting equivalent ionic conductivities as given by (43) such that

$$\lambda_- = \Lambda \frac{\lambda_-^o}{\lambda_-^o + \lambda_+^o} \qquad [88]$$

Once the ionic equivalent conductivities were determined as a function of the KOH concentration and temperature, the ionic free-stream diffusivities were calculated from

$$D_i = \frac{RT\lambda_i}{F^2} \qquad [89]$$

The solubilities of oxygen and hydrogen gas in KOH solutions have been investigated by many investigators (44-49), and the solubility data are usually reported in the form of Setschenow salt effect parameters. This information was used to derive the following correlations for the Henry law constants as a function of temperature and concentration, giving

$$H_i = \frac{(2C_e + C_o)x_i}{1 - x_i} (i = H_2, O_2) \qquad [90]$$

where the mole fractions in the solution are given by

$$x_{O_2} = \frac{1}{\exp\left[-4.1741 + \dfrac{1.3104 \times 10^4}{T} - \dfrac{3.4170 \times 10^6}{T^2} + \dfrac{2.4749 \times 10^8}{T^3}\right] 10^{(0.1923-0.10\times10^{-3}T)1000C_e}} \qquad [91]$$

and

$$x_{H_2} = \frac{\exp\left[-48.1611 + \dfrac{5528.45}{T} + 16.8893 \ln \dfrac{T}{110}\right]}{10^{129.0C_e}} \qquad [92]$$

and the solvent concentration is given by the thermodynamic relation

$$1 = C_e \bar{V}_e + C_o \bar{V}_o \qquad [93]$$

Based on these correlations, the reference concentrations needed in the Butler-Volmer electrochemical reactions were determined, as shown in Table III. Table III also contains the partial molar volumes of the electrolyte and the solvent (water). These partial molar volumes, assumed constant for this work, were obtained from (33)

$$\bar{V}_e = \frac{M_e - \dfrac{\partial \rho}{\partial C_e}}{\rho - C_e \dfrac{\partial \rho}{\partial C_e}} \qquad [94]$$

for the partial molar volume of the electrolyte and

$$\bar{V}_o = \frac{M_o}{\rho - C_e \dfrac{\partial \rho}{\partial C_e}} \qquad [95]$$

for the partial molar volume of the solvent. The density of the electrolyte, as given by Akerlof and Bender (50), was correlated with temperature and concentration so that the change in density with concentration, $\partial \rho/\partial C_e$, could be determined. Using the base-case operating conditions, the partial molar volumes for the electrolyte and the solvent were then calculated using Eq. [94] and [95], respectively, as shown in Table III. The transference number for the OH⁻ ion with respect to the solvent velocity, $t_-^o$, introduced into the volume-average velocity expression, Eq. [59], was determined by

$$t_-^o = \frac{\lambda_-}{\lambda_- + \lambda_+} \qquad [96]$$

where it is assumed constant over the electrolyte concentration range.

## Method of Solution

The alkaline fuel cell model consists of 25 governing equations and 36 outer and internal boundary conditions. These equations are highly coupled and nonlinear and require a numerical method for their solution. The model equations were discretized by using second-order accurate finite-difference approximations (51, 52) in the governing equation regimes and by first-order accurate finite-difference expressions at the boundaries. This switch from second-order to first-order accurate finite-difference expressions at boundaries was necessary to keep a stable solution of the system of equations. The resulting finite difference approximations have a banded matrix structure that can be solved by Newman's BAND(J) algorithm (33).

As the alkaline fuel cell model approaches the limiting current, the dissolved oxygen concentration becomes prohibitively small ($\sim 10^{-9}$ mol/cm³) and creates numerical difficulties with other terms that are of a much higher order of magnitude. The dissolved oxygen concentration was logarithmically transformed in order to achieve limiting current densities with the model. A logarithmically transformed variable, $C_{O_2}^*$ can be defined by

$$C_{O_2}^* = \ln \left(\frac{C_{O_2}}{C_{O_2}^r}\right) \qquad [97]$$

so that the derivatives become

$$\frac{\partial C_{O_2}}{\partial z} = C_{O_2}^r \exp (C_{O_2}^*) \frac{\partial C_{O_2}^*}{\partial z} \qquad [98]$$

for the first derivative and

$$\frac{\partial^2 C_{O_2}}{\partial z^2} = C_{O_2}^r \exp (C_{O_2}^*) \left[\frac{\partial^2 C_{O_2}^*}{\partial z^2} + \left(\frac{\partial C_{O_2}^*}{\partial z}\right)^2\right] \qquad [99]$$

for the second derivative. Equations [97]-[99] can thus be substituted into the model equations for the dissolved oxygen concentration.

To prevent forcing the electrolyte out of the separator, the total pressure drop across the separator was forced to zero by adjusting the fraction $f_a$. Since a potentiostatic approach is used to model the alkaline fuel cell, the cell potential is set, and the current density is calculated by the model. Convergence is obtained when the predicted cell current density is equal in all regions of the fuel cell, as expressed by Eq. [25] for the electrode potentials in the gas-diffusion regions, Eq. [60] for the integral of the local current densities in the gas reaction regions, by

$$\frac{I_{cell}}{nF} = -N_i^g \ (i = O_2, H_2) \qquad [100]$$

for the gas-diffusion regions, and

$$I_{cell} = F \sum z_i N_i \quad (i = +, -) \qquad [101]$$

for the separator.

## Results and Discussion

The base case-parameters shown in Tables I to III were used with the alkaline fuel cell model to calculate the eleven dependent variables as a function of cell potential and spatial domain. The cell potential was varied over the potential range of 1.1 to 0.7 V, representative of the activation-to-concentration polarization range, respectively. These variables were then used to predict the current density as a function of cell potential. The variation of the electrolyte concentration throughout the reaction layers and the separator is shown in Fig. 2 over the potential range of 0.7 to 1.1 V. Since the electrolyte does not circulate outside the fuel cell, the model assumes that no loss or production of the initial charge of electrolyte will occur. That is, the total number of moles of KOH is assumed to remain constant in the fuel cell. Previous models (27, 31) for porous gas-diffusion electrodes have typically neglected this electrolyte concentration variation. This simplification is reasonable at low current densities, as shown by the relatively constant electrolyte concentration at high cell potentials in Fig. 2. However, at low cell potentials, an approximately 1.2*M* change results in the electrolyte concentration from the anode to the cathode. This large variation has a significant impact on the evaporation of water and on the physical properties of the species present. Based on the equilibrium expression for the water vapor, Eq. [30], more water vapor will be present in the anode at low cell potentials than at high potentials. The accumulation of water vapor in the anode could flood the electrode at low cell potentials, degrading the performance of the system. In the cathode regions, the larger electrolyte concentration at low cell potentials causes less water vapor to be present, which could dry out the electrode. Figure 2 also shows a fairly constant profile in the 0.7- to 0.8-V potential range, indicating that the electrolyte concentration does not become a limiting factor in the limiting-current region.
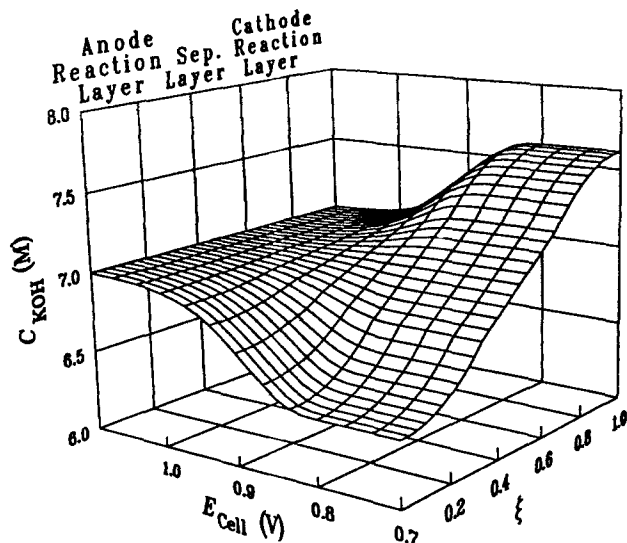
Fig. 2. Variation of the electrolyte concentration across the dimensionless reaction layers and separator.

Fig. 4. Dissolved hydrogen concentration throughout the dimensionless anode and separator regions.

The solubility of oxygen and hydrogen gas in KOH, as given in terms of Henry's law constants, Eq. [90], are noticeably dependent on the electrolyte concentration, as shown in Fig. 3 and 4, respectively. The dissolved oxygen concentration steadily decreases in the cathode reaction region as the cell potential is lowered, reaching an exceedingly small value (on the order of $1.0 \times 10^{-7}M$) at cell potentials lower than 0.85 V. This decrease in the dissolved oxygen concentration results from an increasing consumption of dissolved oxygen by the electrochemical reaction, Eq. [34], and by a decrease in the solubility with increasing electrolyte concentration. Similar results occur for the dissolved hydrogen concentration, as shown in Fig. 4, where the dissolved hydrogen concentration attains a steady value of about $0.36 \times 10^{-3}M$ at cell potentials lower than 0.85 V. Comparing Fig. 3 and 4 shows that the low concentration of dissolved oxygen at potentials lower than 0.85 V causes mass-transfer limitations in the cathode. Therefore, in order to obtain high current densities, more dissolved oxygen is needed in the cathode. The model of a single electrode by Ref. (31) predicts that the dissolved oxygen diffusion contributes the least amount to the polarization losses. However, this result was obtained for a low current density of 200 mA/cm$^2$. At this current density, the AFC model predicts an appreciable amount of dissolved oxygen present in the electrolyte, so that diffusional resist-
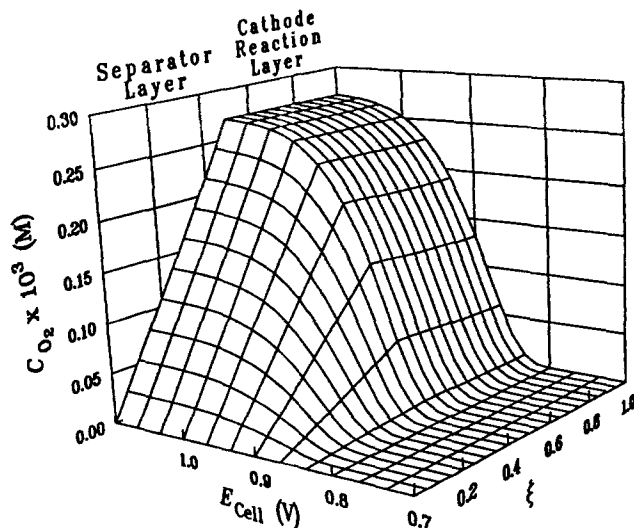
ances of dissolved oxygen are not as significant as at the limiting current.

The transfer rates associated with three cell potentials are shown in Fig. 5, where the transfer rates increase in magnitude from the gas diffusion/reaction interfaces to the separator. The location and distribution of the reaction zone has been investigated by (9, 53), where it is has been concluded that most of the electrochemical reaction occurs within a 0.01-cm distance in the catalyst layer as measured from the gas-diffusion layer. However, in addition to obtaining the optimal reaction-layer thicknesses, it is equally important to determine the distribution of the current throughout the reaction regions. As shown in Fig. 5, the transfer currents have a significant variation across the 0.005-cm-thick reaction layers. Since the transfer currents are large near the separator, more electrocatalysts could be distributed near the diffusion/reaction interfaces to increase the reaction rates at these points. Optimizing the catalyst distribution with respect to the

Fig. 3. Dissolved oxygen concentration throughout the dimensionless separator and cathode regions.

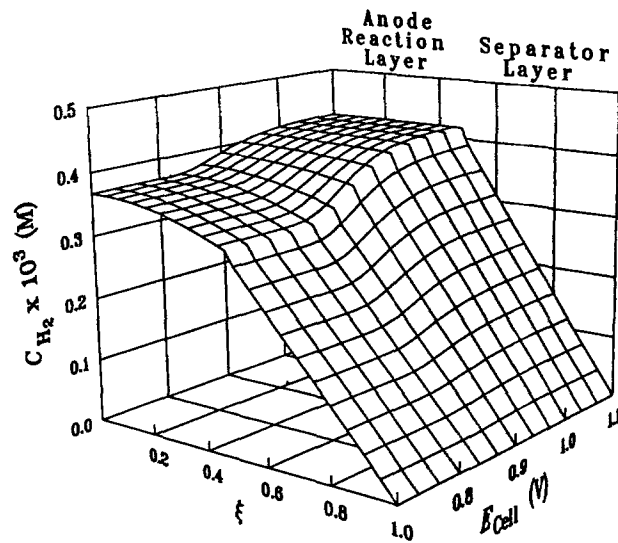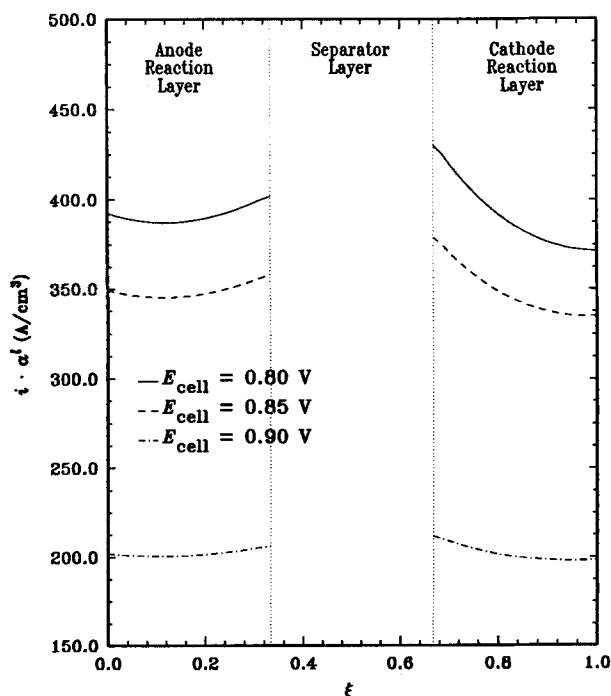Fig. 5. Variation of the anodic ($i_a \cdot a_a^l$) and cathodic ($-i_c \cdot a_c^l$) transfer currents for various cell potentials.
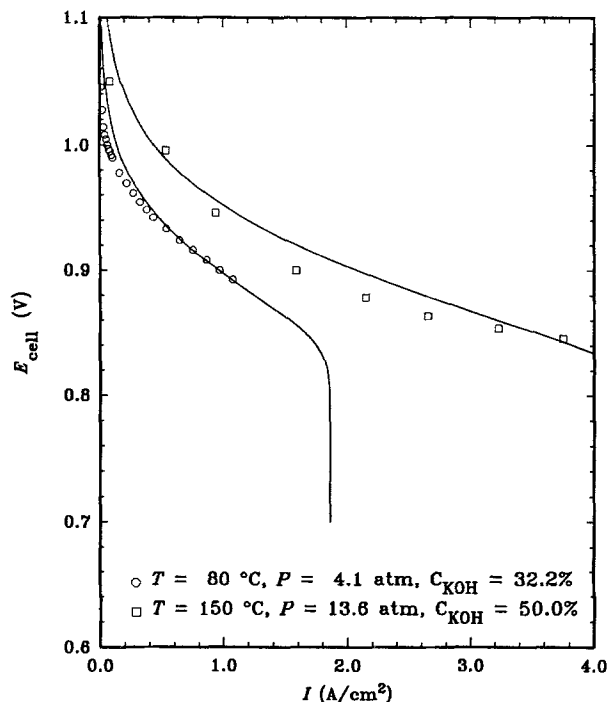
Fig. 6. Comparison of the model (—) and experimental predictions of the alkaline fuel cell polarization.
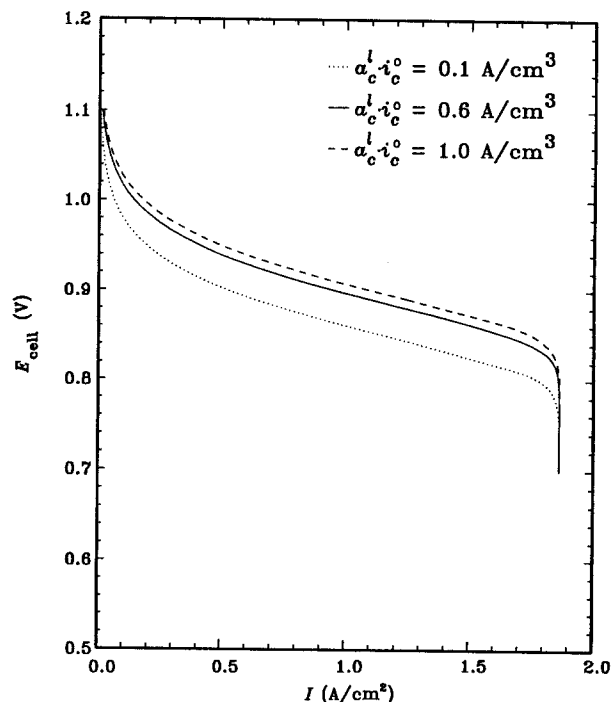


Fig. 7. Effects of the cathodic exchange transfer current on the alkaline fuel cell polarization.

current density, amount of catalyst material, and cost could yield an improved electrode performance.

For comparison purposes, the models' predicted polarization is shown with some experimental polarization data (54) for two sets of operating conditions in Fig. 6. The parameters shown in Table I were used for the low temperature and pressure polarization in Fig. 6. Close agreement is obtained between the predicted and experimental polarization results. Since the complete operating conditions and fuel-cell specifications are not given by Ref. (54) for the experimental results, an accurate comparison between the model and experimental results cannot be made. Parameter estimation could be used to fit the model to the experimental data if more experimental information were known. This would allow the model to predict accurately the fuel-cell performance beyond the experimental domain. Note that the model predictions for the high pressure and temperature polarization in Fig. 6 only cover part of the experimental data range. This is due to some inaccuracies of the transport property correlations at high temperatures and pressures. Obtaining reliable experimental data for the various transport properties at high temperatures and pressures would improve the model's ability to predict high-performance results for a wider range of operating conditions.

The model predictions in Fig. 6 are influenced by four parameters: the anodic and cathodic exchange transfer currents ($i_a^o \cdot a_a^l$ and $i_c^o \cdot a_c^l$) and the anodic and cathodic diffusional film areas ($a_a^g/\delta_a$ and $a_c^g/\delta_c$). These parameters can significantly influence the polarization, as shown in Fig. 7 for different values of the cathodic exchange transfer current. This parameter is shown to influence the activation polarization region of the system without influencing the slope of the ohmic polarization region or the limiting current density at all. This suggests that an appreciable increase in the fuel cell performance up to the limiting current density can be obtained by increasing the electrocatalytic activity. Since the model predicts the same limiting current density for increasing exchange transfer currents, the dissolved oxygen concentration has to become even smaller to offset the higher exchange current densities. Similar results, as shown in Fig. 7, were obtained for different anodic exchange transfer currents.

The effects of different cathodic and anodic diffusional film areas are shown in Fig. 8. Two benefits are achieved by increasing the cathodic diffusional film-area parameter.

First, the slope of the ohmic polarization is minimized, allowing larger current densities to be obtained and, second, the limiting current density is increased. Increasing $a_c^g/\delta_c$ is associated directly with increasing the oxygen gas dissolution rate as given by Eq. [13]. Hence, in order to obtain high current densities, the number of gas-liquid sites should be increased, allowing more gas to dissolve into the electrolyte. Note that this does not necessarily imply that more gaseous-filled pores should be present in the three-phase electrode. That is, increasing the gas-phase porosity in the reaction layer, $\epsilon_R^g$, will increase the number of gaseous-
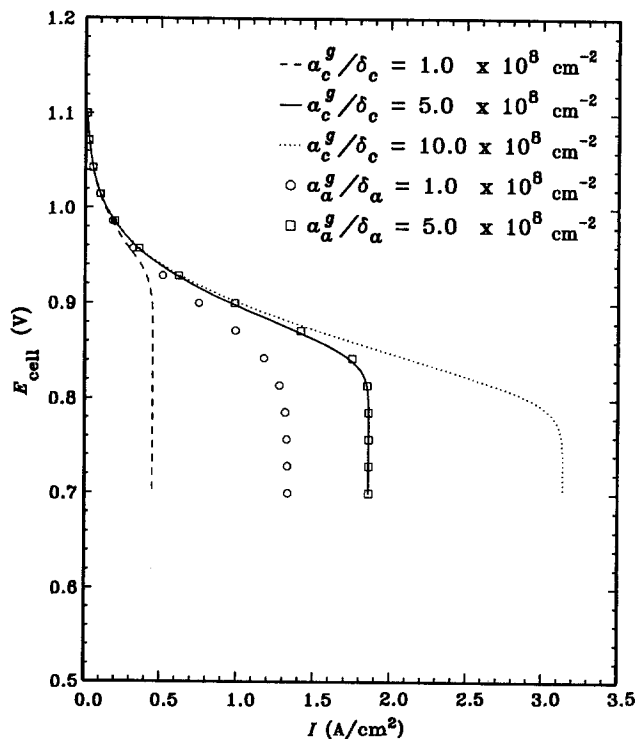


Fig. 8. Influence of the cathodic and anodic diffusional film area parameters on the fuel cell polarization.
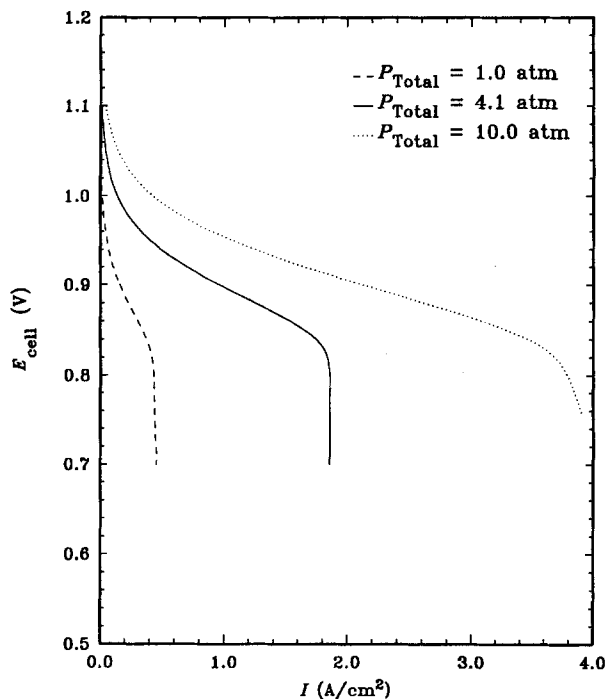
Fig. 9. Pressure effects on the alkaline fuel cell polarization evaluated under the base-case conditions.



Fig. 10. Temperature effects on the alkaline fuel cell polarization evaluated under the base-case conditions.

filled pores, but not necessarily the gas-phase specific surface area, $a^g$. Figure 8 also shows the polarization for two anodic diffusional film areas. Doubling this parameter from the base-case value of $5 \times 10^8$ cm$^{-2}$ does not show any change from the base-case polarization (shown by the solid line in Fig. 8). This simply indicates that the oxygen dissolution rate is limiting the performance. However, when $a_a^g/\delta_a$ is lowered to $1.0 \times 10^8$ cm$^{-2}$, the resulting performance decreases indicating that the hydrogen dissolution process is rate-controlling. These results indicate that a significant interaction can occur between the anode and cathode in controlling the polarization. The ability to investigate the interaction of the anode, separator, and cathode is one advantage to using a complete model of the alkaline fuel cell rather than using single-electrode models as previously done.

To investigate the alkaline fuel cell under different operating conditions, the effects of different pressures and temperatures on the polarization are shown in Fig. 9 and 10, respectively. Increasing the system pressure is shown to improve the performance by decreasing the activation, ohmic, and concentration polarizations. Hence, the mass-transfer limitations due to the low dissolved oxygen concentration can be diminished by operating the fuel cell at a higher pressure. As shown in Fig. 9, increasing the temperature increases the activation polarization while extending the limiting current density. Operating the alkaline fuel cell at higher temperatures can improve the system performance. Since the temperature has a significant impact on the cell performance, the inclusion of a thermal balance into a future alkaline fuel cell model could improve the model predictions.

In order to determine the major limitations to alkaline fuel cell performance, the base-case conditions were used to examine the performance when certain forms of resistance were neglected, as shown in Fig. 11, where the percent increase in the predicted current densities over the base-case current densities is shown. To accomplish this, the various transport parameters were set to large values such that a further increase in the transport parameter would not change the resulting polarization. Thus, to investigate the effects of no gas-phase resistances, the gaseous diffusivities were set to $\approx 10,000$ so that no gas-phase transport resistances would exist. In an analogous manner, other transport parameters were increased, to minimize their respective form of resistance. As shown in
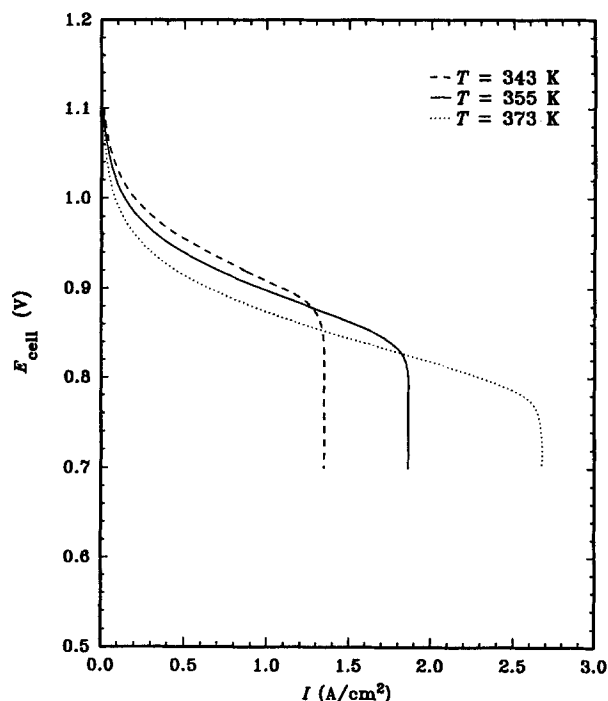
Fig. 11, minimizing gas-phase diffusional resistances will contribute the least to improving the performance. Ionic resistance effects were minimized by increasing the conductivity of the electrolyte, which gave a better performance increase than neglecting gas-phase diffusional resistances. The common assumption of no electronic drop is shown in Fig. 11 to give the highest increase in performance for cell potentials greater than 0.9 V. However, for cell potentials lower than 0.9 V, the solution-phase resistances have the most influence on the performance. This is reasonable, since at potentials that approach the limiting cur-
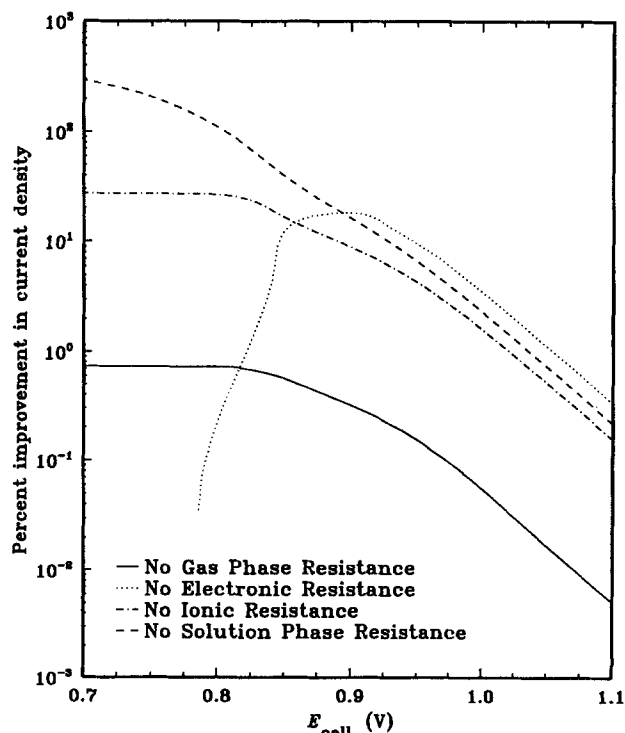


Fig. 11. Improvement in the current density with respect to the base-case current density ($i - i_{base}/i_{base} \times 100$) when different forms of resistance are neglected.

rent density, mass-transfer effects prevent the attainment of even higher current densities. Increasing the liquid-phase diffusion rates and the solubilities of the reactant gases will increase the alkaline fuel cell performance at low cell potentials.

## Summary

A mathematical model of an alkaline fuel cell has been developed to predict the performance of the system for different cell potentials operating under steady-state and isothermal conditions. The model describes the phenomena occurring in the gas, liquid, and solid phases of the anode and cathode gas diffusion regions, the anode and cathode reaction layers, and the separator. The model accounts for the one-dimensional transport of reactant gases, water vapor, solution-phase concentrations, solid and solution potential variations, and the volume-average velocity. Performance results were obtained for a set of base-case conditions that could be used for a high-performance alkaline fuel cell. Gas-phase diffusional resistances were found not to significantly influence the performance of the system. The model predicts that the diffusion of dissolved oxygen contributes the most to the polarization losses at low potentials, while the electronic resistances contribute the most resistance at high cell potentials. To obtain better performance with the alkaline fuel cell, it is suggested that the three-phase electrodes should be highly conductive and contain a large number of gas-liquid sites, allowing more reactant gas to dissolve into the electrolyte. Increasing the pressure and temperature will also result in improved performance.

Various attributes of the system, such as the catalyst distribution, exchange transfer currents, and diffusional film areas, could be optimized to yield better performance. The model shows that interactions between the anode and cathode exist, suggesting that models or experiments based on full cells are necessary, instead of half-cells, when estimating unknown parameters or optimizing various attributes. One of the main advantages of this model is its ability to show quantitatively the influence of different parameters on the predicted current density. These quantitative results can help in the design of alkaline fuel cells, as well as help focus the direction of future research on alkaline fuel cells.

## Acknowledgment

## LIST OF SYMBOLS

| | |
|---|---|
| $a^g$ | specific gas-phase surface area, cm²/cm³ |
| $a^l$ | specific liquid-phase surface area, cm²/cm³ |
| $b$ | Tafel slope, V/decade |
| $C_i$ | concentration of species $i$, mol/cm³ |
| $D_i$ | free-stream diffusivity of species $i$, cm²/s |
| $\mathcal{D}_i$ | effective diffusivity of species $i$, cm²/s |
| $E$ | electrode potential, V |
| $F$ | Faraday's constant, 96,487 C/mol |
| $f_a$ | fraction of water generated that leaves through the anode |
| $H_i$ | Henry's law constant for species $i$, mol/(cm³atm) |
| $I$ | total cell current density, A/cm² |
| $i$ | local current density, A/cm² |
| $i^o$ | exchange current density, A/cm² |
| $M_i$ | molecular weight of species $i$ |
| $n$ | number of electrons transferred |
| $N_i$ | flux of species $i$, mol/(cm²/s) |
| $P_i$ | pressure of species $i$, atm |
| $p_i$ | anodic reaction order for species $i$ |
| $q_i$ | cathodic reaction order for species $i$ |
| $R$ | gas constant, 8.314 J/(mol-K) or 82.057 cm³atm/(mol-K) |
| $R_i^e$ | electrochemical reaction rate, mol/(cm³-s) |
| $R_i^p$ | transport rate across phase boundary, mol/(cm³-s) |

| | |
|---|---|
| $s_i$ | stoichiometric coefficient of species $i$ |
| $t$ | time, s |
| $t_i^o$ | transference number of species $i$ relative to the solvent velocity |
| $T$ | temperature, K |
| $U$ | theoretical open-circuit potential evaluated at reference concentrations, V |
| $U^\theta$ | standard electrode potential, V |
| $U_{RE}^\theta$ | reference electrode potential, V |
| $u_i$ | mobility of species $i$, cm²mol/(J-s) |
| $\bar{V}_i$ | partial molar volume of species $i$, cm³/mol |
| $x_i$ | liquid-phase mole fraction of species $i$ |
| $y_i$ | vapor-phase mole fraction of species $i$ |
| $z$ | spatial coordinate, cm |
| $z_i$ | charge number of species $i$ |

### Greek

| | |
|---|---|
| $\alpha_a$ | anodic transfer coefficient |
| $\alpha_c$ | cathodic transfer coefficient |
| $\delta$ | diffusion layer thickness, cm |
| $\epsilon$ | porosity |
| $\eta$ | overpotential, V |
| $\Lambda$ | equivalent conductance, cm²/Ω · eq. |
| $\lambda_i^o$ | limiting ionic conductivity of species $i$, cm²/Ω · eq. |
| $\lambda_i$ | ionic conductivity of species $i$, cm²/Ω · eq. |
| $\nu_i$ | number of anions or cations produced by the dissociating electrolyte |
| $\rho$ | electrolyte density, g/cm³ |
| $\sigma$ | electrode conductivity, S/cm² |
| $\tau$ | tortuosity |
| $\phi$ | solution-phase potential, V |

### Superscripts

| | |
|---|---|
| e | electrochemical rate |
| g | gas phase |
| l | liquid phase |
| r | reference condition |
| p | production rate due to transport across a phase boundary |
| T | total value |
| o | solvent (water) |
| * | logarithmically transformed variable |

### Subscripts

| | |
|---|---|
| a | anode |
| c | cathode |
| D | diffusion layer |
| e | electrolyte |
| i | species $i$ |
| R | reaction layer |
| S | separator layer |
| o | solvent (water) |
| + | cation ($K^+$) |
| − | anion ($OH^-$) |

## REFERENCES

1. S. Srinivasan, *This Journal*, **136**, 41C (1989).
2. K. Tomantschger, S. Srinivasan, R. D. Findlay, I. Joanes, F. McClusky, L. Oporto, A. Reid, and K. Kordesch, Paper 859370, 20th Intersociety Energy Conversion Engineering Conference (1985).
3. H. V. Broeck, "Fuel Cell Seminar," abstracts, p. 125, Tucson, AZ, May 19-22, 1985.
4. J. O'M. Bockris and S. Srinivasan, "Fuel Cells: Their Electrochemistry," McGraw-Hill, New York (1969).
5. L. Swette and J. Giner, *J. Power Sources*, **22**, 399 (1988).
6. K. Tomantschger, F. McClusky, L. Oporto, and A. Reid, *ibid.*, **18**, 317 (1986).
7. W. M. Vogel and K. A. Klinedinst, *Electrochim. Acta*, **22**, 1385 (1977).
8. S. Srinivasan and E. Gileadi, in "Handbook of Fuel Cell Technology," C. Berger, Editor, Prentice-Hall, Inc., Englewood Cliffs, NJ (1968).
9. T. Kenjo and K. Kawatsu, *Electrochim. Acta*, **30**, 229 (1985).
10. L. Müller and L. N. Nekrasov, *ibid.*, **9**, 1015 (1964).
11. L. Müller and L. N. Nekrasov, *J. Electroanal. Chem.*, **9**, 282 (1965).
12. A. Damjanovic, M. A. Genshaw, and J. O'M. Bockris, *J. Phys. Chem.*, **70**, 3761 (1966).
13. A. Damjanovic, M. A. Genshaw, and J. O'M. Bockris, *This Journal*, **114**, 1107 (1967).
14. A. Kozawa, *J. Electroanal. Chem.*, **8**, 20 (1964).
15. R. J. Bowen and H. B. Urbach, *J. Chem. Phys.*, **49**, 1206 (1968).

16. E. Yeager, *Electrochim. Acta,* **29,** 1527 (1984).
17. K. Mund, G. Richter, and F. von Sturm, in "The Electrocatalysis of Fuel Cell Reactions," (PV 79-2) W. E. O'Grady, S. Srinivasan, and R. F. Dudley, Editors, p. 47, The Electrochemical Society Softbound Proceedings Series, Pennington, NJ (1979).
18. W. Vielstich, *ibid.,* p. 67.
19. J. Appleby and R. K. Sen, *ibid.,* p. 84.
20. D. B. Sepa, M. V. Vojnovic, and A. Damjanovic, *Electrochim. Acta,* **25,** 1491 (1980).
21. A. J. Appleby and J. Marie, *ibid.,* **24,** 195 (1979).
22. R. DeLevie, in "Advances in Electrochemistry and Electrochemical Engineering," Vol. 6, P. Delahay, Editor, p. 329, Interscience Publishers Inc., New York (1967).
23. Y. A. Chizmadzhev and Y. G. Chirkov, in "Comprehensive Treatise of Electrochemistry," Vol. 6, E. B. Yeager, J. O'M. Bockris, B. E. Conway, and S. Sarangapani, Editors, p. 317, Plenum Press, New York (1983).
24. B. V. Tilak, R. S. Yeo, and S. Srinivasan, *ibid.,* Vol. 3, p. 39 (1981).
25. K. V. Kordesch, *This Journal,* **125,** 77C (1978).
26. J. Newman and W. Tiedemann, *AIChE J.,* **21,** 25 (1975).
27. J. Giner and C. Hunter, *This Journal,* **116,** 1124 (1969).
28. H. R. Kunz, L. J. Bregoli, and S. T. Szymanski, *ibid.,* **131,** 2815 (1984).
29. H. R. Kunz and L. A. Murphy, *ibid.,* **135,** 1124 (1988).
30. M. B. Cutlip, *Electrochim. Acta,* **20,** 767 (1975).
31. R. P. Iczkowski and M. B. Cutlip, *This Journal,* **127,** 1433 (1980).
32. R. B. Bird, W. E. Stewart, and E. N. Lightfoot, "Transport Phenomena," John Wiley & Sons, New York (1960).
33. J. S. Newman, "Electrochemical Systems," Prentice-Hall, Inc., Englewood Cliffs, NJ (1973).
34. D. M. Bernardi, *This Journal,* **137,** 3344 (1990).
35. K. V. Kordesch, in "Handbook of Fuel Cell Technology," C. Berger, Editor, Prentice-Hall, Inc., Englewood Cliffs, NJ (1968).

36. R. E. White, S. E. Lorimer, and R. Darby, *This Journal,* **130,** 1123 (1983).
37. S. G. Bratsch, *J. Phys. Chem. Ref. Data,* **18** (1989).
38. J. Newman and T. W. Chapman, *AIChE J.,* **19,** 343 (1973).
39. L. G. Austin, in "Handbook of Fuel Cell Technology," C. Berger, Editor, Prentice-Hall, Inc., Englewood Cliffs, NJ (1968).
40. W. L. Fielder and J. Singer, Abstract 66, p. 107, The Electrochemical Society Extended Abstracts, Vol. 90-2, Seattle, WA, Oct. 14-19, 1990.
41. M. K. Tham, R. D. Walker, and K. E. Gubbins, *J. Phys. Chem.,* **74,** 1747 (1970).
42. L. S. Darken and H. F. Meier, *J. Am. Chem. Soc.,* **64,** 621 (1942).
43. D. Dobos, "Electrochemical Data," Elsevier, Amsterdam, The Netherlands (1975).
44. M. B. Knaster and L. A. Apel'baum, *Russ. J. Phys. Chem.,* **38,** 120 (1964).
45. K. E. Gubbins and R. D. Walker, *This Journal,* **112,** 469 (1965).
46. P. Ruetschi and R. F. Amlie, *J. Phys. Chem.,* **70,** 718 (1966).
47. R. E. Davis, G. L. Horvath, and C. W. Tobias, *Electrochim. Acta,* **12,** 287 (1967).
48. S. K. Shoor, R. D. Walker, and K. E. Gubbins, *J. Phys. Chem.,* **73,** 312 (1969).
49. C. L. Young, "IUPAC Solubility Data Series," Vol. 5/6, Pergamon Press, New York (1981).
50. G. Akerlof and P. Bender, *J. Am. Chem. Soc.,* **63,** 1085 (1941).
51. B. A. Finlayson, "Nonlinear Analysis in Chemical Engineering," McGraw-Hill, New York (1980).
52. W. J. Minkowycz, E. M. Sparrow, G. E. Schneider, and R. H. Pletcher, "Handbook of Numerical Heat Transfer," John Wiley & Sons, New York (1988).
53. P. Bjornbom, *Electrochim. Acta,* **32,** 115 (1987).
54. R. E. Martin and M. A. Manzo, Paper 889498, 23rd Intersociety Energy Conversion Engineering Conference (1988).

# Design of Alloy Electrocatalysts for CO₂ Reduction

## III. The Selective and Reversible Reduction of CO₂ on Cu Alloy Electrodes

**Masahiro Watanabe,\* Masami Shibata, and Akihiro Kato**

*Laboratory of Electrochemical Energy Conversion, Faculty of Engineering, Yamanashi University, Takeda, Kofu 400, Japan*

**Masashi Azuma**

*Department of Applied Chemistry, Osaka Institute of Technology, Asahi-ku, Osaka 535, Japan*

**Tadayoshi Sakata**

*The Graduate School at Nagatsuda, Tokyo Institute of Technology, Midori-ku, Yokohama 227, Japan*

### ABSTRACT

Many Cu alloys have been studied for electrocatalytic activity of $CO_2$ reduction in $0.05M$ $KHCO_3$ aqueous solution. Anomalously low overpotentials with highly selective Cu alloy catalysts have been seen for the reduction of $CO_2$ to $CH_3OH$, $HCOOH$, or CO. Cu-Ni alloys produce $CH_3OH$ and $HCOOH$ selectively at reversible potentials and Cu-Sn and Cu-Pb produce $HCOOH$ and CO with an enhanced reaction rate at the reversible potentials of formation. Other alloy catalysts such as Cu-Zn, Cu-Cd, or Cu-Ag also exhibit behaviors distinct from those of the elemental metals. The results reported here indicate further possibilities for the development of powerful new electrocatalysts for the reduction of $CO_2$.

Electrochemical reduction of carbon dioxide has been studied on metal electrodes both in aqueous solutions (1-7) and in nonaqueous solutions (8). The previous works have shown that $CO_2$ is reduced at high Faradaic efficiency to HCOOH on electrodes such as Hg (2-6), Pb (5, 6), and In and Zn (5-7). CO is formed on Ag and Au electrodes (5) in aqueous solutions. Copper electrodes have shown high Faradaic efficiencies for methane and ethylene production

for $CO_2$ (5, 9-11). We have investigated the electrochemical reduction of $CO_2$ at about 0°C in aqueous $KHCO_3$ solution on 32 metal electrodes (12, 13). It was found that the faradaic efficiency for electroreduction of $CO_2$ increased significantly on lowering the temperature, and that the major reduction products formed on these metal electrodes showed systematic changes when they were arranged in the periodic table of corresponding elemental metals (13). From these previous studies, the behavior of pure metals for $CO_2$ electroreduction has been fairly well

\*Electrochemical Society Active Member.